ELSEVIER

Check for updates

Graphite nanocrystals coated paper-based electrode for detection of SARS-Cov-2 gene using DNA-functionalized Au@carbon dot core–shell nanoparticles

Mohammad Ali Farzin [a], Hassan Abdoos [a,*], Reza Saber [b]

[a] Department of Nanotechnology, Faculty of New Sciences and Technologies, Semnan University, P.O. Box: 35131-19111, Semnan, Iran
[b] Department of Medical Nanotechnology, School of Advanced Technologies in Medicine, Tehran University of Medical Sciences, Tehran, Iran

ARTICLE INFO

ABSTRACT

Currently, the development of biosensors is an urgent need due to the rapid spread of SARS-CoV-2 and the limitations of current standard methods for the diagnosis of COVID-19. Hence, many researchers have focused on the design of high-performance biosensors for measuring coronavirus genes. In this study, a voltammetric genosensor was developed for the determination of SARS-CoV-2 RdRP gene based on the format of cDNA probe/ Au@CD core–shell NPs/graphite nanocrystals (GNCs)/paper electrode. For the first time, graphite nanocrystals were used in the electrochemical biosensor design. This genosensor was exposed to different concentrations of virus gene and then the hybridization between cDNA probe and RdRP gene was monitored by redox-active to-luidine blue (TB). With increasing the RdRP concentration, the reduction peak current of TB enhanced in a linear range of 0.50 pM-12.00 nM according to the regression equation of I (μA) = 7.60 log C_{RdRP} (pM) + 25.78. The repeatability with a RSD of 2.2% clearly exhibited that the response of modified electrode is stable because of the high adhesion of GNC layer on the paper substrate and the high stability of cDNA-Au@CD bioconjugates. The spike-and-recovery studies showed the acceptable recoveries for the sputum samples (>95%).

1. Introduction

The pandemic of coronavirus disease 2019 (COVID-19) caused by the SARS-CoV-2 still remains a global threat [1]. Millions of people have died from this disease, and many of them continue to suffer from symptoms long after their initial infection is gone. Regarding the high rate of transmission of this viral infection and the involvement of all countries in the world, it is necessary to make fundamental decisions to manage this fatal viral disease. The most important practical step in this regard is to break the chain of infection transmission between infected and susceptible people in the community, which requires fast and reliable diagnosis methods for the accurate viral detection. At present, the qualitative reverse transcription-polymerase chain reaction (RT-PCR) assay as a nucleic acid amplification test is the most common method for the detection of different virus genes, especially nucleocaspid (N), envelope (E) and RNA-dependent RNA polymerase (RdRP) genes [2–4]. However, the possibility of both false-negative and false-positive errors should be considered in the interpreting of RT-PCR tests. The false-positive results can arise from contamination with previously

amplified DNA [5]. While, the false-negative errors can result in the viral RNA degradation during transport or storage, poor sample collection and low virus concentrations [6]. The large number of both false-negative and false-positive errors reduce the reliability of this method. Therefore, it is necessary to refine the current available tests for the sensitive and reliable diagnosis of SARS-CoV-2, aiming to control and prevent large outbreak of COVID-19.

The electrochemical genosensors are an alternative method for detection of viral genes, due to excellent sensitivity, high selectivity, simplicity and low limit of detection (LOD). More importantly, they don't require amplification processes as the RT-LAMP or RT-PCR [7]. Combining the sensing strategies and nanotechnology can make these analytical diagnostic tools more efficient. In particular, the use of AuNPs and carbon-based nanomaterials in the design of electrochemical genosensors leads to the sensing technology evaluation. Numerous research articles published annually on metal NPs and carbon nanomaterials as the electrocatalysts or electron-transfer accelerators confirms this claim [8–11].

The unique characteristics of AuNPs to provide a large surface area

for the loading of bioreceptors without losing their bioactivity and to facilitate electron transfer on the electrode surface have led to the widespread utility of these nanoparticles for improving the analytical performance of electrochemical sensors [12–14]. However, small sized AuNPs tend to form larger nanoparticle aggregates [15]. Thus, it is critical to prevent the aggregation of particles using the appropriate capping (stabilizing) agents during the synthesis of AuNPs [16]. The suitable choice of stabilizing agent not only affects the shape and size of nanoparticles but can also play an important role in the electrochemical performance of AuNPs. The semiconductor carbon quantum dots (CQDs) or carbon dots (CDs) have been well documented as the stabilizing and reducing agents [16,17]. They have been recognized as a novel generation of carbon-based nanomaterials with high solubility, low toxicity, great electronic features, large surface areas and lots of edge sites for functionalization [18]. An effective approach for overcoming the inherent limitations of AuNPs and CDs as the nanoplatforms in the fabrication of electrochemical biosensors is to combine them in the nanocomposite form [19]. These Au-C nanocomposites provide enhanced sensitivity and low LOD in the electrochemical nano-biosensors especially paper-based sensors [19].

Paper-based biosensors suggest low-cost substrates for detection of biological species in the clinical samples. Despite the unique advantages such as low-cost, disposability and biocompatibility, the electrical conductivity of the cellulose paper is not sufficient for use in electrochemical sensors [20]. A number of methods have been utilized to deposit conductive materials on a substrate including filtration, sputtering, printing methods, etc [21]. Here for the first time, a conductive graphite nanocrystal (GNC) layer as a transition state between graphite and tetrahedral amorphous carbon (TAC) grew on the cellulose paper substrate by ion beam sputtering deposition (IBSD) method. Due to the monoenergetic and highly collimated ion beam, the obtained coating is usually extremely dense and adheres effectively to the substrate. This leads to the formation of durable, stable and high-quality films by this method compared to the vapor deposition technology [22]. According to the results obtained in this study, the formed GNC layer has a high capacity to increase the paper surface as well as increase its electrical conductivity.

2. Experimental

2.1. Reagents and chemicals

Dried borage (starflower) herb was prepared from Ramsar (Mazandaran, Iran) and powdered prior to use. Thiourea, bovine serum albumin (BSA), toluidine blue (TB), *N*-hydroxysuccinimide (NHS), disodium hydrogen phosphate (Na_2HPO_4), potassium ferricyanide ($K_3Fe(CN)_6$), sodium tetrachloroaurate ($NaAuCl_4$), 1-ethyl-3-(3-dimethylamino-propyl)carbodiimide (EDC), sodium dihydrogen phosphate (NaH_2PO_4) and potassium ferrocyanide ($K_4Fe(CN)_6 \cdot 3H_2O$) were also obtained from Sigma-Aldrich.

The interfering and target oligonucleotides, consisting the SARS RdRP gene (5′-C CAGGT GGAAC ATCAT CCGGT GATGC-3), SARS-CoV-2 envelope (E) gene (5′-ACAC TAGCC ATCCT TACTG CGCTT CG-3′), SARS-CoV-2 RdRP gene (5′-CAGGT GGAAC CTCAT CAGGA GATGC-3′) and single-base mismatch strand (5′-CA<u>C</u>GT GGAAC CTCAT CAGGA GATGC-3′) were purchased by Faza Pajooh (Tehran, Iran) according to the previous reports [23–26].

2.2. Fabrication of GNC/paper electrode

At the beginning of the experiment, the filter paper was oven-dried for 3 h at 105 °C. Then, a thin film of GNC was coated on the paper surface by the sputtering of SIGRACELL® bipolar plates produced from high purity graphite (>99%, 12 cm × 15 cm). The main characteristic of natural graphite is high resistance to chemicals and good electrical conductivity. The specific angle between the paper and graphite plate

was about 45°. The pressure was kept constant during deposition at 2×10^{-5} Torr by the introduction of high purity argon gas (99.999% purity). To achieve the desired pressure, the vacuum pump of 200 W rating should be run for approximately 1 h. During this time, no sputtering takes place and the power is only expended on creating a vacuum in the chamber. The ion current, accelerator voltage and deposition time were 25 mA, 2200 V and 45 min, respectively. After deposition process, the coated paper substrate was cooled in an argon atmosphere to room temperature. Finally, for preparation of working electrode, the GNC/paper was cut to 10 mm × 6 mm dimensions [27].

2.3. Green N, S-co-doped CD synthesis

Typically, the powdered borage herb was utilized as a carbon source for preparation of N,S-doped CDs with thiourea as a nitrogen and sulfur source. 0.5 g of borage powder, 1.0 g of thiourea and 40 mL of distilled water were transferred into a Teflon-lined stainless steel autoclave and sealed. Then, the autoclave was put into a preheated (180 °C) oven for 6 h similar to another reports in which citric acid or dopamine were used as raw materials under the hydrothermal route [28,29]. After that, the resulting brown solution centrifuged and filtered. Then, the solvent was eliminated by a rotary evaporator.

2.4. Production of Au@CD core–shell NPs

For preparation of a stock solution (2 mg mL^{-1}), the powder N,S-doped CDs were re-dissolved into the distilled water. Then, the Au@CD core–shell NPs were synthesized following a procedure reported in the previous article with minor modifications [16]. Briefly, 1 mL of the N,S-doped CDs stock solution was added dropwise to 10 mL of $NaAuCl_4$ solution (1.0 mM) at 95 °C under vigorous stirring to form the reddish brown Au@CD core–shell NPs. The N,S-doped CDs as the mild reducing agents can be lead to the reduction of Au(III).

2.5. Development of signal-on genosensor

The Au@CD core–shell NPs were deposited on the GNC/paper electrode to obtained Au@CD NPs/GNC/paper. The obtained modified electrode was oven-dried for 3 h at 60 °C. Then, a solution including 1 mM of EDC, 2 mM of NHS and 5 mM was dropped on the Au@CD NPs/GNC/paper electrode and remained for 30 min at room temperature. Finally, the modified paper-based electrode was dipped in the aminated cDNA (10 μM) solution for 1 h. In this step, the functional groups of carboxyl on the CDs were activated by an EDC/NHS cross-linker [30]. To decrease the non-specific binding, a 0.25% BSA solution was pipetted on the modified electrode and dried at room temperature.

The electrochemical sensing assay for RdRP detection is based on a signal-on mechanism. The cDNA/Au@CD NPs/GNC/paper electrode was exposed to different amounts of RdRP standards at room temperature for 40 min and then rinsed with distilled water to separate the unhybridized strands. To detect the DNA hybridization, TB as a heterocyclic aromatic dye which binds to nucleic acids was used in the genosensor fabrication. This hybridization indicator interacts electrostatically with negatively charged backbone phosphate groups. In addition, TB interacts with small grooves of ssDNA or ssRNA via hydrophobic effects, while it intercalate into the large grooves of dsDNA or dsRNA through π–π stacking and forms hydrogen bonds with bases in the major grooves [31]. So, TB can be used for the discrimination of hybridization reaction. It has stronger affinity with dsDNA compared to the ssDNA [31–33]. Here, 1 mM of TB solution was placed on the RdRP/cDNA/Au@CD NPs/GNC/paper electrode and incubated for 20 min. Then, the voltammetry currents of the designed genosensor were taken in 0.1 M PBS (pH 7.4) for detection of target strands.

The differential pulse voltammetry (DPV) measurements were carried out using a PGSTAT 302 N electrochemical workstation (Autolab, Netherlands) in a three-electrode cell consisting of a Pt auxiliary
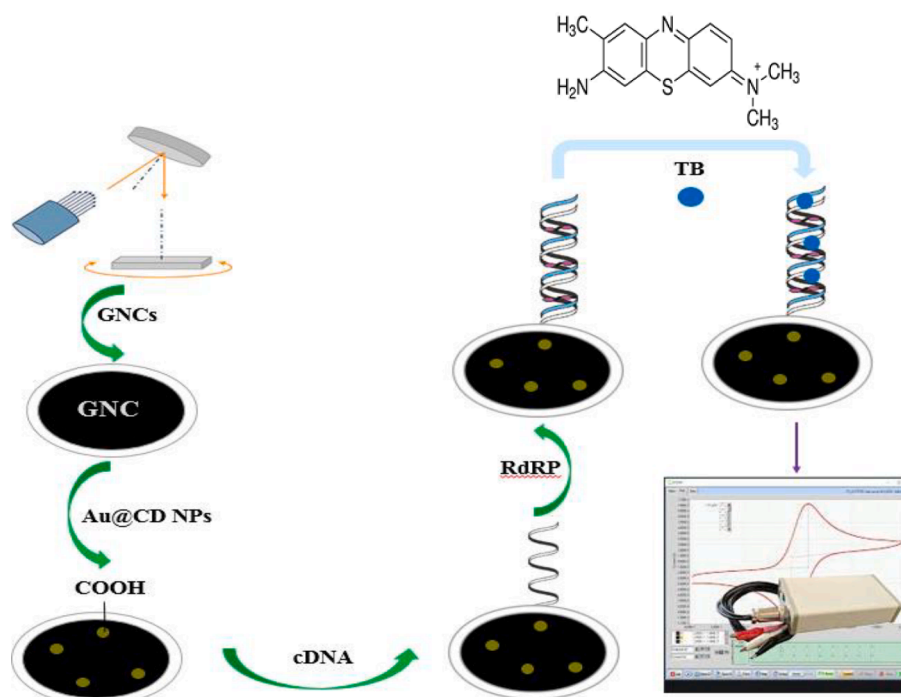
Fig. 1. Schematic illustration of electrochemical genosensor format used in this work.

electrode, an Ag/AgCl (KCl, 3 M) reference electrode and a filter paper-based working electrode. The instrumental parameters was as follows: (I) potential range was from − 0.4 to 0.0 V, (II) pulse amplitude was 0.05 V, (III) pulse width was 0.06 s and (IV) sample width was 0.02 s.

Fig. 1 presents the schematic illustration of electrochemical genosensor format used in this work.

3. Results and discussion

3.1. Characterization of GNC/paper electrode

To determine morphology, the scanning electron microscope (SEM) images of pristine paper (Fig. 2A and 2B) and GNC deposited on the paper (Fig. 2C and 2D) were conducted with various magnification levels using an EVO 18 microscope (ZEISS, Germany). These images revealed the formation of graphite nanoflakes on the cellulose fibers of filter paper. In addition, the SEM study of deposited GNC film showed a morphology similar to that of nanocrystals synthesized in previous papers [34,35].

Raman spectroscopy, as one of the most common analytical techniques, determines the structure and the bonding nature of carbonaceous nanomaterials. Here, dispersive Raman microscope (DRM) system (Bruker, Germany) was applied for the characterization of GNCs. The confocal depth resolution of 2 μm allows individual layers of GNCs to be analyzed separately.

In general, the spectrum of all carbon nanomaterials consists of two Raman bands (D and G), except for natural graphite which has a single Raman active mode (G) at 1580 cm^{-1}. The G-band (1550–1570 cm^{-1}) is related to the stretching vibration of C = C (sp^2) on unsaturated compounds such as aromatic rings or olefinic chains (both rings and chains) [36,37], while the disorder induced D-band (1370 cm^{-1}) as a breathing mode is strongly related to the six-membered aromatic rings [38]. Therefore, no rings, no D peak [39]. The analysis of Raman spectrum of as-prepared carbon nanomaterial indicates the two distinct bands D (1370 cm^{-1}) and G (~1600 cm^{-1}) with the intensity ratio (I_D/I_G) of 2 (Fig. 3). According to Ferrari's amorphization trajectory (Three-stage model of the variation of the Raman G position and the I_D/I_G with enhancing disorder) [39,40], the produced nanomaterial which is in the end of stage 1 corresponds to graphite nanocrystals. The evolution of the Raman spectrum in stage 1 is as follows: D band becomes clear and I_D/I_G increases (inset of Fig. 3). Although the D peak is absent in ordered graphite, it appears with decreasing grain size and consequently disorderity increasing. The crystallization of graphite leading to decrease in grain size [41]. In this stage, the G band position moves from 1580 cm^{-1} to 1600 cm^{-1}. The G-peak wavenumber or frequency shifts upward as the grain size decreases [42].

3.2. Characterization of N, S-co-doped CDs

To survey the optical characteristics of N,S-doped CDs, the UV–vis absorption and fluorescence spectra of the as-synthesized CDs were taken on UV-1700 spectrophotometer (Shimadzu, Japan) and LS 55 photo luminescence spectrometer (Perkin Elmer, USA) at the room temperature, respectively. The UV–vis absorption of the as-synthesized N,S-doped CDs demonstrated a band at about 345 nm (Fig. S1A), which is characteristic of the CDs [43]. In addition, the maximal fluorescence emission intensity was detected at an emission wavelength of 412 nm and an excitation wavelength of 320 nm (Fig. S1B). The N,S-doped CD solution under a laser lamp appeared blue (inset of Fig. S1B), due to Tyndall effect [44]. To investigate the morphology and size of the N,S-doped CD solution, transmission electron microscope (TEM) image of CD solution was recorded on an EM10C instrument (ZEISS, Germany). As seen in Fig. S1C, the N,S-CDs were spherical with an average size of ~ 10 nm. The particle size of N,S-doped CD solution was also confirmed by detection of hydrodynamic diameter (D_H) using Nano ZS90 (Malvern Instruments, UK). The size distribution showed a sharp peak around 10 nm (inset of Fig. S1C). To identify molecular structure such as bond and functional group, the Fourier transform infrared (FT-IR) spectrum of the N,S-doped CD was recorded (Fig. S1D) using a Vector 22 spectrometer (Brucker Corporation, Germany). The absorption band at 3456.2 cm^{-1} was related to the O–H bond stretching vibrations, while the strong peaks at 2850.5 and 2923.8 cm^{-1} show the presence of CH$_2$ groups. These results confirms the chain structure of the N,S-doped CDs. The observed intense band at 1743.5 cm^{-1} is due to the stretching vibration of C = O functional group. In addition, the characteristic absorption band at 1168.7 cm^{-1} originates from C-N vibration.
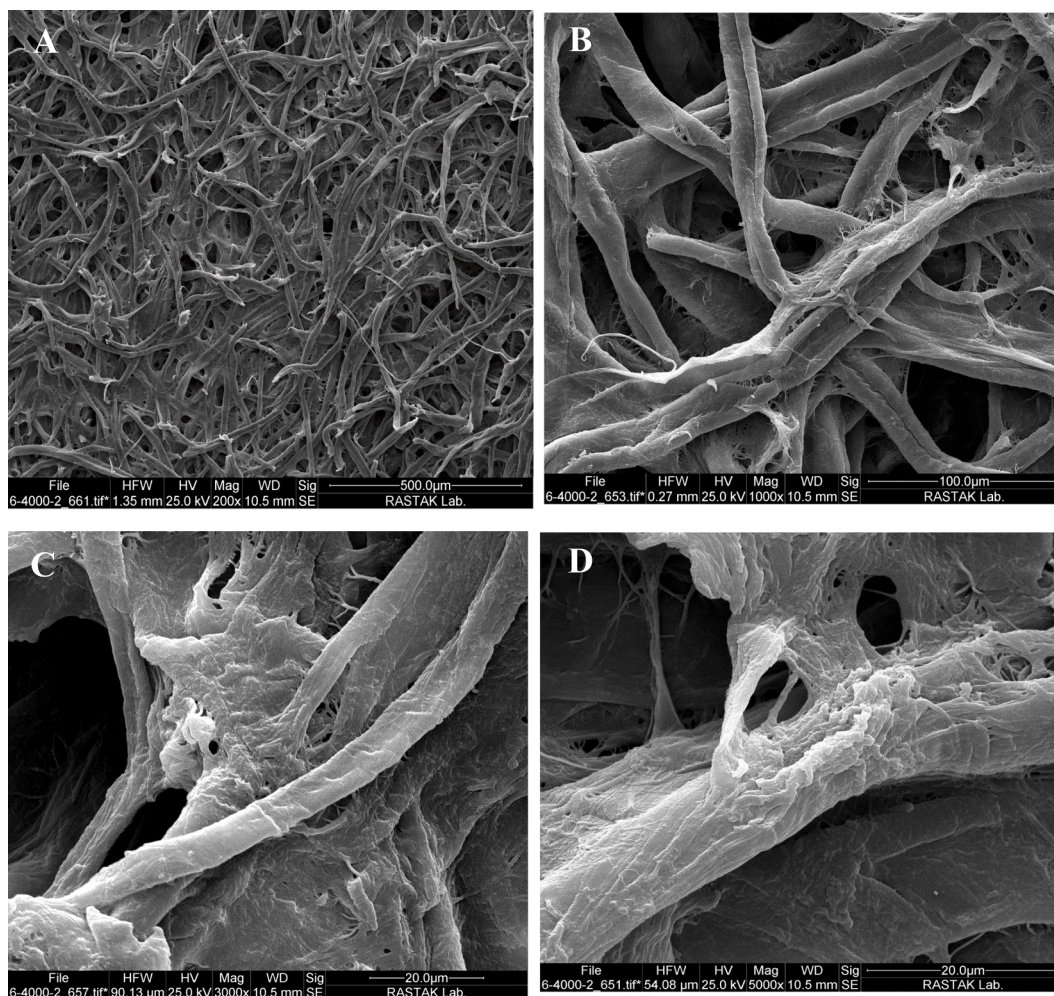
Fig. 2. SEM images of (A) pristine paper with magnification of 200x, (B) pristine paper with magnification of 1000x, (C) GNCs deposited on the paper with magnification of 3000x and (D) GNCs deposited on the paper with magnification of 5000x.
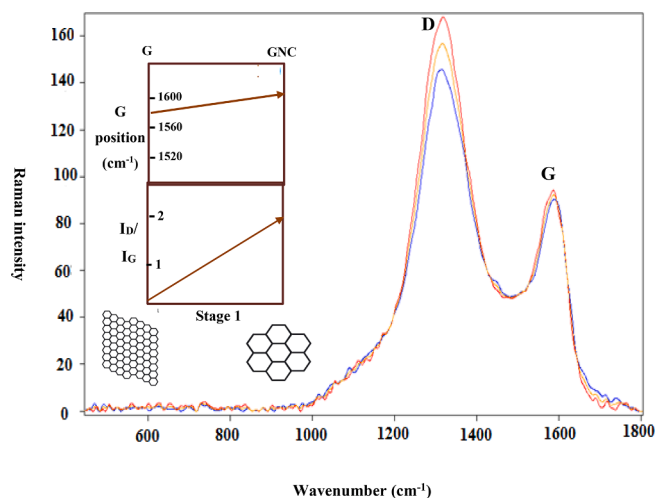
Fig. 3. Raman spectrum of GNC produced by IBSD; inset of this image shows amorphization trajectory consisting stage 1 from graphite (G) to graphite nanocrystals (GNC) [39,40].

The absorption at 1548.7 cm^{-1} is attributed to the skeleton vibration of C = N in the triazine ring [45]. The strong peak at 1639.3 cm^{-1} is assigned to the stretching vibration of C = C. The C-S stretching
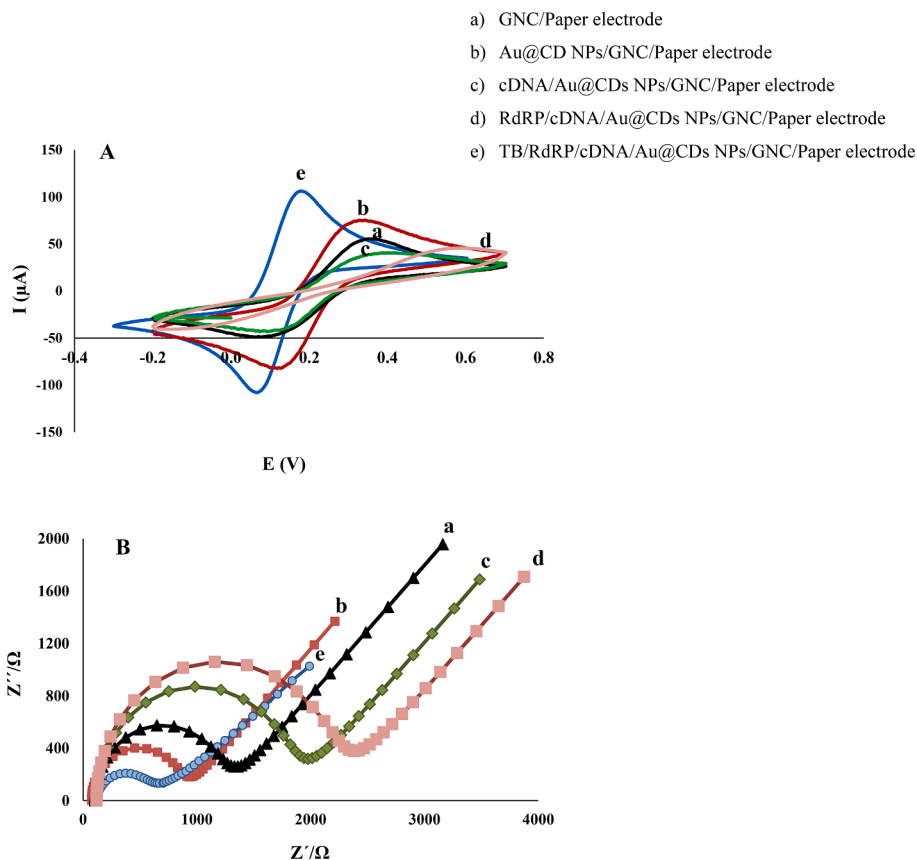
vibration is related to a weak peak at 621.0 cm^{-1} [46]. Other peaks at 715.5 and 1461.9 cm^{-1} reflect the absorption of C–H bond vibration. Our results are consistent with those of the previous published literature [42].

3.3. Characterization of Au@CD core–shell NPs

The morphology of N,S-doped CDs was surveyed by TEM. As seen in Fig. S2A, the average size of quasi-spherical CDs was approximately 30 nm. The DLS intensity-based size distribution histogram confirmed this particle size. The DLS result showed an average D_H of ~ 30 nm (inset of Fig. S2A). Unlike N,S-doped CDs, a wide range of size distribution was observed for Au@CD NPs due to the use of a mild reducing agent. In general, strong reducing agents such as $NaBH_4$ induces instant nucleation, while CDs as a mild reducing agent leads to producing the AuNPs with a wide range of size distribution [16]. The UV–vis absorbance spectrum of AuNPs was surveyed (Fig. S2B) and showed a characteristic surface plasmon peak at ~ 525 nm. This result suggests the formation of red AuNPs (inset of Fig. S2B) through the reduction of $AuCl_4$ by N,S-doped CDs. The elemental composition of nanoparticles was investigated by EDX technique. The obtained spectrum indicates the presence of Au, S and N (Fig. S2C).

3.4. Characterization of Au@CD NPs/GNC/paper electrode

SEM was utilized to provide information concerning the morphology

a) GNC/Paper electrode
b) Au@CD NPs/GNC/Paper electrode
c) cDNA/Au@CDs NPs/GNC/Paper electrode
d) RdRP/cDNA/Au@CDs NPs/GNC/Paper electrode
e) TB/RdRP/cDNA/Au@CDs NPs/GNC/Paper electrode

Fig. 4. (A) CV curves and (B) Niquist plots of (a) GNC/paper electrode, (b) Au@CD NPs/GNC/paper electrode, (c) cDNA/Au@CDs NPs/GNC/paper electrode, (d) RdRP/cDNA/Au@CDs NPs/GNC/paper electrode and (e) TB/RdRP/cDNA/Au@CDs NPs/GNC/paper electrode in 0.1 M KCl containing 5 mM $Fe(CN)_6^{3-/4-}$.

of Au@CD NPs/GNC/paper electrode surface. Fig. S3 showed that the described approach could lead to homogeneous formation of Au@CD NPs on the GNC modified electrode surface.

3.5. Electrochemical behaviors of different modified electrodes

The electrochemical response of electrode was investigated after each modification step using the cyclic voltammetry (CV) in the $Fe(CN)_6^{3-/4-}$ solutions as the electroactive indicator (Fig. 4A). As observed, the peak current of Au@CD NPs/GNC/paper electrode (curve b) increased significantly compared to the GNC/paper electrode (curve a). This confirms that the deposition of Au@CD NPs on the modified electrode increases the electrical conductivity and thus encourages the electron transfer rate [31,47]. So, the Au@CD core–shell NPs can greatly amplify the biosensor signals. The peak current clearly decreased when the cDNA was added to the electrode surface (curve c) due to the electrostatic repulsion. The negative charge of DNA strands caused by the presence of phosphate groups in their backbones leads to repel of signal probe from the electrode surface [46]. In addition, DNA as a non-conductive oligonucleotide chain creates an insulting layer on the electrode surface [31,48]. With the introduction of negatively-charged RdRP strands (12 nM), the peak current further increased (curve d), while the conjugation of positively-charged TB (1 mM) with DNA-DNA duplex led to dramatic increase in the peak current and negative shift of peak potential (curve e). The obtained result is explained by electrostatic attraction between TB and signal probe. TB, as an electroactive indicator, was utilized for the detection of the hybridization reaction on the electrode surface.

Electrochemical impedance spectroscopy (EIS) is also a convenient approach for investigation of surface changes of electrode during the modification process. To support the CV results, the Nyquist plots were collected at a bias potential of 0.18 V (Fig. 4B). The impedance of the bare GNC/paper electrode was acquired (curve a), which represents a small semicircle. When the Au@CD NPs were casted on the electrode surface, the R_{ct} reduced significantly (curve b) due to the high electrical conductivity of metallic nanoparticles. The immobilization of cDNA on the Au@CD NPs/GNC/paper electrode led to a considerable increase in R_{ct} (curve c). The non-conductive cDNA strands acted as a mass-transfer blocking barrier, thus insulating the electrode surface and preventing the electroactive indicator from reaching the electrode surface [48]. After the hybridization of cDNA with the RdRP gene, the R_{ct} indicated a further enhancement (curve d) due to the thickening of the insulting film and the electrostatic repulsion between dsDNA and signal probe. Finally, the R_{ct} decreased significantly upon the interaction of electroactive TB with the dsDNA (curve e), as a result of electrostatic attraction between positively-charged TB and negatively-charged $Fe(CN)_6^{3-/4-}$.

3.6. Optimization of genosensor performance

To survey the influence of experimental effective parameters on the genosensor signal, the DPV current of the TB (1 mM) intercalated into the cDNA-RdRP (10 pM) duplex was measured under the following conditions: (I) deposition time varied in the range of 30 min to 1 h, while the accelerator voltage and the ion current were kept constant (2200 V and 25 mA, respectively); (II) the Au@CD NPs/GNC/paper electrode was dipped into the aminated cDNAs (bioreceptor strands) with different concentrations from 1 μM to 12 μM; (III) 1 mM of TB solution as the hybridization indicator was placed on the RdRP/cDNA/Au@CD NPs/GNC/paper electrode and incubated for different times from 5 min to 20 min.

The bar charts of DPV currents of the accumulated hybridization indicator on the modified electrode indicated the optimum desorption
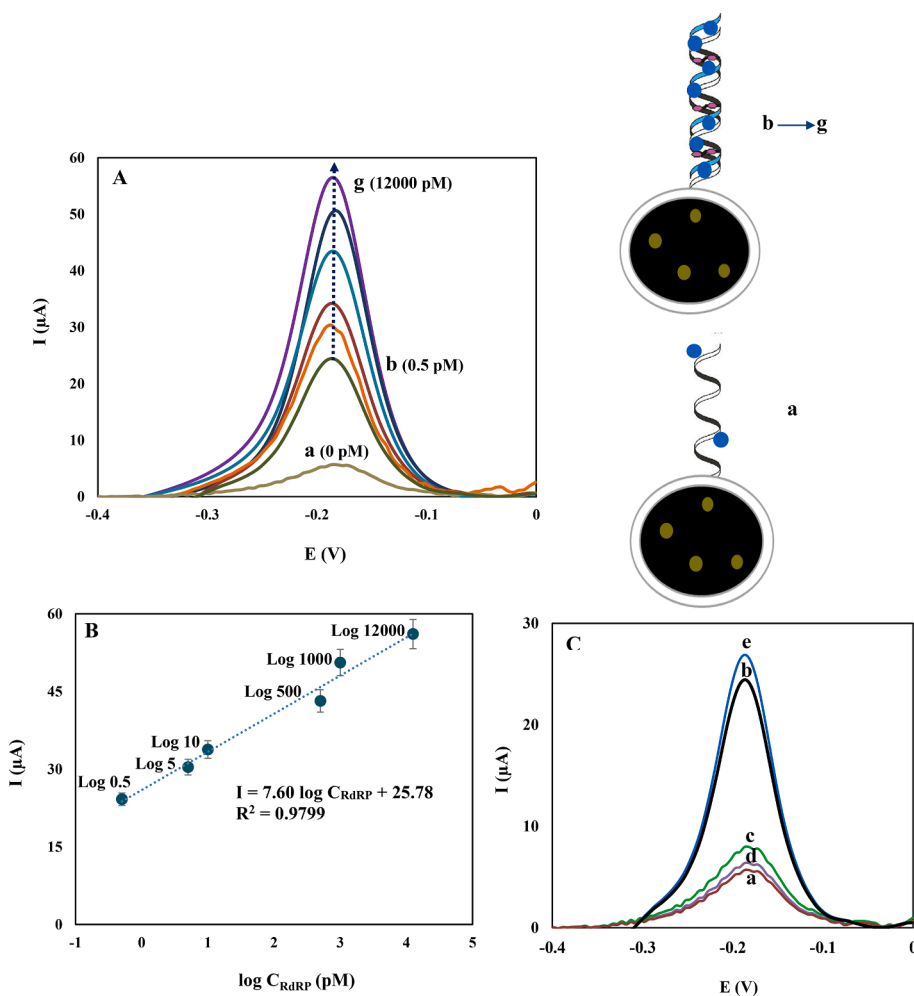
Fig. 5. (A) DPVs of cDNA/Au@CD NPs/GNC/paper electrode into (a) 0 pM, (b) 0.5 pM, (c) 5 pM, (d) 10 pM, (e) 500 pM, (f) 1000 pM, (g) 12000 pM of SARS-CoV-2 RdRP gene and TB (1 mM) in 0.1 M PBS of pH 7.4; (B) Calibration curve of I_p versus log C_{RdRP}; (C) DPVs of cDNA/Au@CDs NPs/GNC/Paper electrode in 1 mM of TB indicator and (a) PBS of pH 7.4, (b) SARS-CoV-2 RdRP gene (10 pM), (c) SARS RdRP gene (100 pM), (d) E gene (100 pM) and (e) a mixture of target (10 pM) and interfering (10-fold) genes.

time of 45 min (Fig. S4A). In less times, the graphite nanocrystals have not yet formed and the main material is in the form of graphite. At higher times, the G peak shifts to lower wavenumbers [49]. The blue shift of G band caused by reducing the number of ordered aromatic rings contributes to the passing from graphite nanocrystals to amorphous carbon [50]. With increasing desorption time from 45 min to 1 h, graphite nanocrystals were formed in a bed of amorphous carbon. So, the TB current decreased due to the reduction of electrode surface and electrical conductivity.

The peak current of hybridization indicator intensified with enhancing the concentration of immobilized cDNA strands on the surface of Au@CD NPs/GNC/paper electrode up to 10 μM (Fig. S4B). However, the higher amounts of cDNA strands resulted in the saturation of electrode surface and thus steric resistance [48].

The peak current of TB intercalated into the dsDNA enhanced with overtime from 5 to 20 min (Fig. S4C). Further increase of the accumulation time did not change the indicator signal.

3.7. Investigation of analytical figure of merits

The important figures of merit to be considered for validating SARS-CoV-2 RdRP biosensor were investigated by the DPV method in the potential interval of −0.4–0 V. To achieve this aim, the proposed genosensor was exposed to different concentrations of RdRP and then the hybridization between the immobilized cDNA probe and target gene was monitored by a redox-active indicator. As seen in Fig. 5A, a very small peak was recorded in the absence of target sequences due to the interaction of TB (1 mM) with small grooves of probe ssDNA through

hydrophobic effects. With the addition of RdRP sequences (0.5 pM) to the cDNA/Au@CD NPs/GNC/paper electrode, a significant peak was recorded because of TB intercalation into the large grooves of cDNA-RdRP duplex through JI-JI stacking. These observations show that TB has a stronger affinity with dsDNA compared to the ssDNA. The addition of different amounts of SARS-CoV-2 RdRP to the cDNA/Au@CD NPs/GNC/paper electrode surface led to different increases in the peak current of the TB indicator. Based on such signal-on strategy, the developed genosensor showed the acceptable responses to different concentrations of RdRP gene in a dynamic linear range (DLR) of 0.50 pM-12.00 nM with a regression equation of I (μA) = 7.60 log C_{RdRP} (pM) + 25.78 (R^2 = 0.9799) (n = 6) (Fig. 5B). The limit of detection (LOD) and limit of quantification (LOQ) assessed as $3S_b$/m and $10S_b$/m were 0.15 pM and 0.50 pM, respectively.

The peak current stability of TB/RdRP/cDNA/Au@CD NPs/GNC/paper electrode was surveyed in 0.1 M PBS solution (pH 7.4). To achieve this aim, 5 repetitive DPV peaks of TB reduction were recorded. The relative standard deviation (RSD) for the voltammogram currents was calculated as 2.2%. Thus, this outcome obviously exhibited that the response of modified electrode is stable because of the high adhesion of GNCs on the paper substrate and the high stability of cDNA-Au@CD NPs bioconjugate.

For estimation of reproducibility, 5 modified electrodes were fabricated with the same protocol and utilized to measure 10 pM of RdRP gene. The RSD for 5 independent measurements was evaluated at 8.1%.

The specificity of the cDNA sequence immobilized on the Au@CD NPs/GNC/paper electrode towards different sequences including SARS RdRP gene (100 pM), SARS-CoV-2 E gene (100 pM) and SARS-CoV-2

Table 1

Spike-and-recovery method for assessing the accuracy of RdRP biosensor.

Sputum samples	Added gene	[a]Found gene	RSD (%)	Recovery (%)
1	10.0 pM	9.7	2.2	97.0
2	50.0 pM	48.9	1.7	97.8
3	500 pM	490.3	1.4	98.1

[a] Calculated as a mean of four measurements.

RdRP gene (10 pM) was evaluated in the presence of TB (1 mM) using DPV method. Compared to curve a, a significant increase in TB current was observed for curve b, while negligible changes were recorded for curves c and d (Fig. 5C). The response of cDNA/Au@CD NPs/GNC/ paper electrode in the mixture of target (10 pM) and interfering (10-fold) genes indicated a slight increase compared with that of modified electrode for SARS-CoV-2 RdRP (curve e). These achievements confirm the genosensor selectivity towards the SARS-CoV-2 RdRP gene in the presence of SARS RdRP and SARS-CoV-2 E genes. In addition, the selectivity of the current genosensor in the presence of single-base mismatch strand was investigated in the SI.

3.8. Determination of RdRP gene in sputum samples

To validate the accuracy of this protocol, the SARS-COV-2 RdRP sequences were measured in the spiked human sputum samples. These samples were prepared from a healthy volunteer and centrifuged at 5000 rpm for 15 min. Then, the standard addition method or spike-and-recovery was utilized to detect RdRP genes in the diluted sputum samples. To achieve this aim, different amounts of SARS-CoV-2 RdRP gene

(0.5 pM, 10.0 pM and 1000.0 pM) were added to the diluted sputum samples. Each spiked sputum sample was quantified 4 times and the obtained data were presented in Table 1. These outcomes showed the acceptable recoveries for the sputum samples (>95%).

3.9. Performance comparison of the designed RdRP sensing device with the similar genosensors

For better comparison with the performance of other genosensors for the SARS-CoV-2 detection, Table 2 presents figures of merit of the previously reported nanomaterial-based genosensors and the current strategy [26,51–60].

Compared to the reported articles, the analytical performance of developed genosensor in this study is acceptable. Unlike the signal-off trends, our proposed genosensor does not suffer from limitations imposed by the background current [61]. It becomes clear that the performance of electrochemical biosensors depends on the electrode materials and nanoplatforms. In this study, GNC produced by IBSD technique not only increase the effective electrode surface area but also lead to greater sensor stability. These nanocrystals as the efficient interfaces possess excellent adhesion. In fact, the adhesion of coating is best when the carbon film is deposited by IBSD technique [22]. Another advantage of this biosensor is that the Au@CD NPs can be efficiently applied as the signal amplification nanoplatform. More importantly, the paper-based electrodes are very attractive components for the disposable, nontoxic, low-cost and flexible biosensors especially wearable biosensors which require characteristics of paper-based electrodes.

Table 2

Comparison of the analytical performance of different genosensors for SARS-CoV-2 RNA detection.

Detection method	Format of biosensing strategy	LOD	DLR	Real sample	*Total time	Ref.
EC	CPE–HT18C6(Ag)/CHT/SiQDs@PAMAM/cDNA/RdRP gene	0.3 pM	1.0 pM–8.0 nM	Sputum	35 min	[26]
FET	Si/SiO$_2$/RGO/AuNPs/cDNA/RdRP gene	0.37 fM (PBS) 2.29 fM (throat swap) 3.99 fM (serum)	10 fM–10 pM	Throat swab, Serum	64 min	[51]
EC	DEP-Chips/GONCs/cDNA/RdRP gene	186×10^{-9} M	10^{-10}–10^{-5} M	———	35 min	[52]
ECL	GE/DT/DNA$_1$/DNA$_2$/Ru (bpy)$_3^{2+}$ modified DNA$_3$/RdRP gene	2.67 fM	Up to 100 pM	Serum	75 min	[53]
EC	SPE/Au@Fe$_3$O$_4$-CP-HT/ORF1ab gene/SCX8-RGO-Au-TB-LP-AP	3 aM	10^{-17}–10^{-12} M	Sputum, Throat swab, Urine, Plasma, Serum, Feces, Oral swab, Whole blood, Saliva	210 min	[54]
EC	SPE/NC (MoS$_2$NSs, GNPs, CHT)/AuNFs/SA/Biotin-crRNA-MB/Cas13a protein/ORF gene or S gene	4.4×10^{-2} fg mL^{-1} (ORF gene) 8.1×10^{-2} fg mL^{-1} (S gene)	1×10^{-1}–1×10^5 fg mL^{-1}	Artificial saliva	90 min	[55]
ECL	Electrode/PEI-Ru@Ti$_3$C$_2$@AuNPs/DNA7-Fc/AuNP-DNA1-DNA2-DNA3-DNA4/RdRP gene/DNA5/DNA6/CRISPR-Cas12a	12.8 aM	Up to 500 aM	Pharyngeal swab	110 min	[56]
ECL	GCE/AuNPs-g-C$_3$N$_4$/DNA1(Y1, Y2 and Y3)/Hairpin1/Hairpin2/DNA-Ru/RdRP gene	59 aM	Up to 30 fM	Pharyngeal swab	180 min	[57]
ECL	GCE/Nafion/Au@Ti$_3$C$_2$@PEI-Ru(dcbpy)$_3^{2+}$/Hairpin DNA/Swing arm/RdRP gene/Nb.BbvCI/DNA-AgNCs	0.21 fM	1 fM–100 pM	Serum	120 min	[58]
LSPR	ssDNA-functionalized AuNIs/RdRP gene	0.22 pM	———	———	14 min	[59]
NEC	cDNA-AuNPs/N gene	0.18 ng µL^{-1}	———	Oropharyngeal swab	10 min	[60]
EC	Paper electrode/GNC/Au@CD NPs/cDNA/RdRP gene	0.15 pM	0.50 pM-12.00 nM	Sputum	75 min	This work

*Total-time was defined as the sample preparation time until the assay time.

EC: Electrochemistry; CPE: Carbon paste electrode; HT18C6(Ag): Silver-incorporated hexathia-18-crown-6; CHT: Chitosan; SiQDs@PAMAM: Poly(amidoamine) coated silicon quantum dots; RdRP: RNA depended RNA polymerase; FET: Field-effect transistor; DEP-Chips: Disposable electrical printed chips; GONCs: Graphene oxide nanocolloids; ECL: Electrochemiluminescence; GE: Gold electrode; CP: Capture probe; HT; Hexane-1-thiol; ORF: open reading frame; SCX8-RGO: p-sulfocalix[8] arene functionalized reduced graphene oxide; TB: Toluidine blue; LP: Label probe; AP: Auxiliary probe; NC: Nonocomposite; MoS$_2$NSs: MoS$_2$ nanosheets; GNPs: Graphene nanoplates; AuNFs: Gold nanoflowes; SA: Streptavidin; crRNA: Complementary reporter RNA; MB: Methylene blue; S gene: Spike gene; PEI: Poly-ethylenimine; Fc: Ferrocene; CRISPR: Clustered Regularly Interspaced Short Palindromic Repeats; GCE: Glassy carbon electrode; Nb.BbvCI: Nicking endonuclease; DNA-AgNCs: DNA-templated silver nanoclusters; LSPR: Local surface plasmon resonance; AuNIs: Gold nanoislands; N gene: Nucleocaspid gene; NEC: Naked-eye colorimetric GNC: Graphite nanocrystal.

4. Conclusion

In this study, the cDNA-functionalized Au@CD core–shell NPs were designed on the coated paper electrode for the SARS-CoV-2 RdRP detection. The deposited GNC film on the paper substrate allowed the development of a voltammetric genosensor by enhancing the electrical conductivity of substrate as well as increasing the effective electrode surface. Based on the stronger binding affinity of TB to cDNA-RdRP duplex than to cDNA, this redox-active indicator was applied to monitor nucleic acid hybridization. With increasing RdRP concentration, the reduction peak current of TB enhanced in a linear range of 0.50 pM-12.00 nM. The developed signal on genosensor exhibited acceptable LOD, excellent selectivity, good stability and high recovery for spiked sputum samples. Despite these strengths, the modification of electrode involves a series of time-consuming steps.

CRediT authorship contribution statement

Mohammad Ali Farzin: Investigation, Writing – original draft. **Hassan Abdoos:** Supervision, Project administration, Writing – review & editing. **Reza Saber:** Supervision.

Declaration of Competing Interest

The authors declare that they have no known competing financial interests or personal relationships that could have appeared to influence the work reported in this paper.

Appendix A. Supplementary data

Supplementary data to this article can be found online at https://doi.org/10.1016/j.microc.2022.107585.

References

[1] Z. Rahmati, M. Roushani, H. Hosseini, H. Choobin, An electrochemical immunosensor using SARS-CoV-2 spike protein-nickel hydroxide nanoparticles bio-conjugate modified SPCE for ultrasensitive detection of SARS-CoV-2 antibodies, Microchem. J. 170 (2021), 106718.

[2] P.B. van Kasteren, B. van der Veer, S. van den Brink, L. Wijsman, J. de Jonge, A. van den Brandt, R. Molenkamp, C.B.E.M. Reusken, A. Meijer, Comparison of seven commercial RT-PCR diagnostic kits for COVID-19, J. Clin. Virol. 128 (2020), 104412.

[3] V.M. Corman, O. Landt, M. Kaiser, R. Molenkamp, A. Meijer, D.K. Chu, T. Bleicker, S. Brünink, J. Schneider, M.L. Schmidt, D.G.J.C. Mulders, B.L. Haagmans, B. van der Veer, S. van den Brink, L. Wijsman, G. Goderski, J.L. Romette, J. Ellis, M. Zambon, M. Peiris, H. Goossens, C. Reusken, M.P.G. Koopmans, C. Drosten, Detection of 2019 novel coronavirus (2019-nCoV) by real-time RT-PCR, Euro. Surveill. 25 (2020) 2000045.

[4] E. Hamidi-Asl, L. Heidari-Khoshkelat, J.B. Raoof, T.P. Richard, S. Farhad, M. Ghani, A review on the recent achievements on coronaviruses recognition using electrochemical detection methods, Microchem. J. 178 (2022), 107322.

[5] S. Roy, Physicians' dilemma of false-positive RT-PCR for COVID-19: a case report, SN Compr. Clin. Med. (2021) 1–4.

[6] J.N. Kanji, N. Zelyas, C. MacDonald, K. Pabbaraju, M.N. Khan, A. Prasad, J. Hu, M. Diggle, B.M. Berenger, G. Tipples, False negative rate of COVID-19 PCR testing: a discordant testing analysis, Virol. J. 18 (2021) 13.

[7] E.E. Etienne, B.B. Nunna, N. Talukder, Y. Wang, E.S. Lee, COVID-19 biomarkers and advanced sensing technologies for point-of-care (POC) diagnosis, Bioengineering 8 (2021) 98.

[8] C. Zhang, X. Du, Electrochemical sensors based on carbon nanomaterial used in diagnosing metabolic disease, Front. Chem. 8 (2020) 651.

[9] Z. Wang, Z. Dai, Carbon nanomaterial-based electrochemical biosensors: an overview, Nanoscale 7 (2015) 6420–6431.

[10] T. Islam, M.M. Hasan, A. Awal, M. Nurunnabi, A.J.S. Ahammad, Metal nanoparticles for electrochemical sensing: Progress and challenges in the clinical transition of point-of-care testing, Molecules 25 (2020) 5787.

[11] J.M. Pingarrón, P. Yáñez-Sedeño, A. González-Cortés, Gold nanoparticle-based electrochemical biosensors, Electrochim. Acta 53 (2008) 5848–5866.

[12] M. Shamsipur, L. Farzin, M.A. Tabrizi, Ultrasensitive aptamer-based on-off assay for lysozyme using a glassy carbon electrode modified with gold nanoparticles and electrochemically reduced graphene oxide, Microchim. Acta 183 (2016) 2733–2743.

[13] M. Pedrero, P. Yáñez-Sedeño, J.M. Pingarrón, Electrochemical DNA Biosensors: Gold nanoparticle-based electrochemical DNA biosensors (2012) 57–102.

[14] M.A. Tabrizi, M. Shamsipur, R. Saber, S. Sarkar, N. Sherkatkhameneh, Flow injection amperometric sandwich-type electrochemical aptasensor for the determination of adenocarcinoma gastric cancer cell using aptamer-Au@Ag nanoparticles as labeled aptamer, Electrochim. Acta 246 (2017) 1147–1154.

[15] M. Irfan, T. Ahmad, M. Moniruzzaman, S. Bhattacharjee, B. Abdullah, Size and stability modulation of ionic liquid functionalized gold nanoparticles synthesized using *Elaeis guineensis* (oil palm) kernel extract, Arab. J. Chem. 13 (2020) 75–85.

[16] M.K. Mahto, D. Samanta, S. Konar, H. Kalita, A. Pathak, N, S doped carbon dots—Plasmonic Au nanocomposites for visible-light photocatalytic reduction of nitroaromatics, J. Mater. Res. 33 (2018) 3906–3916.

[17] T. Nozaki, T. Kakuda, Y.B. Pottathara, H. Kawasaki, A nanocomposite of N-doped carbon dots with gold nanoparticles for visible light active photosensitisers, Photochem. Photobiol. Sci. 18 (2019) 1235–1241.

[18] M.A. Farzin, H. Abdoos, A critical review on quantum dots: From synthesis toward applications in electrochemical biosensors for determination of disease-related biomolecules, Talanta 224 (2021) 121828.

[19] S. Rahmati, W. Doherty, A.A. Babadi, M.S.A.C. Mansor, N.M. Julkapli, V. Hessel, K. Ostrikov, Carbon-gold nanocomposites for environmental contaminant sensing, Micromachines 12 (2021) 719.

[20] H. Zhang, C. Dou, L. Pal, M.A. Hubbe, Review of electrically conductive composites and films containing cellulosic fibers or nanocellulose, BioRes. 14 (2019) 7494–7542.

[21] Y. Yang, Q. Huang, G.F. Payne, R. Sun, X. Wang, A highly conductive, pliable and foldable Cu/cellulose paper electrode enabled by controlled deposition of copper nanoparticles, Nanoscale 11 (2019) 725.

[22] https://www.sputtertargets.net.

[23] Y. Yang, F. Peng, R. Wang, K. Guan, T. Jiang, G. Xu, J. Sun, C. Chang, The deadly coronaviruses: The 2003 SARS pandemic and the 2020 novel coronavirus epidemic in China, J. Autoimmun. 109 (2020), 102434.

[24] R.K. Kakhki, M.K. Kakhki, A. Neshani, COVID-19 target: A specific target for novel coronavirus detection, Gene Rep. 20 (2020), 100740.

[25] M. Yuce, E. Filiztekin, K.G. Ozkaya, COVID-19 diagnosis—A review of current methods, Biosens. Bioelectron. 172 (2021), 112752.

[26] L. Farzin, S. Sadjadi, A. Sheini, E. Mohagheghpour, A nanoscale genosensor for early detection of COVID-19 by voltammetric determination of RNA-dependent RNA polymerase (RdRP) sequence of SARS-CoV-2 virus, Microchim. Acta 188 (2021) 121.

[27] Q. Lu, T. Su, Z. Shang, D. Jin, Y. Shu, Q. Xu, X. Hu, Flexible paper-based Ni-MOF composite/AuNPs/CNTs film electrode for HIV DNA detection, Biosens. Bioelectron. 184 (2021) 113229.

[28] A. Sharma, J. Das, Small molecules derived carbon dots: synthesis and applications in sensing, catalysis, imaging, and biomedicine, J. Nanobiotech. 17 (2019) 92.

[29] D. Xu, F. Lei, H. Chen, L. Yin, Y. Shi, J. Xie, One-step hydrothermal synthesis and optical properties of self-quenching-resistant carbon dots towards fluorescent ink and as nanosensors for Fe^{3+} detection, RSC Adv. 9 (2019) 8290–8299.

[30] Z. Ji, A. Sheardy, Z. Zeng, W. Zhang, H. Chevva, K. Allado, Z. Yin, J. Wei, Tuning the functional groups on carbon nanodots and antioxidant studies, Molecules 24 (2019) 152.

[31] J. Ding, D. Zhang, Y. Liu, M. Yu, X. Zhan, D. Zhang, P. Zhou, An electrochemical aptasensor for detection of lead ions using a screen-printed carbon electrode modified with Au/polypyrrole composites and toluidine blue, Anal. Methods 11 (2019) 4274–4279.

[32] J. Han, Y. Zhuo, Y. Chai, G. Gui, M. Zhao, Q. Zhu, R. Yuan, A signal amplification strategy using the cascade catalysis of gold nanoclusters and glucose dehydrogenase for ultrasensitive detection of thrombin, Biosens. Bioelectron. 50 (2013) 161–166.

[33] H.W. Gao, P. Qin, C. Lin, Z.M. Shang, W. Sun, Electrochemical DNA biosensor for the detection of Listeria monocytogenes using toluidine blue As a hybridization indicator, J. Iran. Chem. Soc. 7 (2010) 119–127.

[34] V.A. Krivchenko, A.A. Pilevsky, A.T. Rakhimov, B.V. Seleznev, N.V. Suetin, M.A. Timofeyev, A.V. Bespalov, O.L. Golikova, Nanocrystalline graphite: Promising material for high current field emission cathodes, J. Appl. Phys. 107 (2010), 014315.

[35] A.T. Rakhimov, Autoemission cathodes (cold emitters) on nanocrystalline carbon and nanodiamond films: physics, technology, applications, Phys. Usp. 43 (2000) 926.

[36] M. Nakamizo, R. Kammereck, P.L. Walker Jr., Laser Raman studies on carbons, Carbon 12 (1974) 259–267.

[37] A. Farnsworth, G. Chirima, F. Yu, Raman Spectroscopy: A key technique in investigating carbon-based materials, Spectroscopy 36 (2021) 9–14.

[38] A.C. Ferrari, J. Robertson, Interpretation of Raman spectra of disordered and amorphous carbon, Phys. Rev. B 61 (2000) 14095.

[39] A.C. Ferrari, J. Robertson, Raman spectroscopy of amorphous, nanostructured, diamond–like carbon, and nanodiamond, Phil. Trans. R. Soc. Lond. A 362 (2004) 2477–2512.

[40] J. Robertson, Diomond-like amorphous carbon, Mater. Sci. Eng. R 37 (2002) 129–281.

[41] A.S. Bhattacharyya, S.K. Mishra, Raman studies on nanocomposite silicon carbonitride thin film deposited by r.f. magnetron sputtering at different substrate temperatures, J. Raman Spect. 41 (2010) 1234–1239.

[42] L. Chong, H. Guo, Y. Zhang, Y. Hu, Y. Zhang, Raman study of strain relaxation from grain boundaries in epitaxial graphene grown by chemical vapor deposition on SiC, Nanomaterials 9 (2019) 372.

[43] Y. Nie, J. Guo, Y. Deng, W. Weng, Synthesis and application of fluorescent N, S co-doped carbon dots based on on-off-on quenching mode for the collaboration detection of iron ions and ascorbic acid, J. Saudi Chem. Soc. 24 (2020) 865–873.

[44] S. Ahmadian-Fard-Fini, D. Ghanbari, O. Amiri, M. Salavati-Niasari, Green sonochemistry assisted synthesis of hollow magnetic and photoluminescent MgFe$_2$O$_4$–carbon dot nanocomposite as a sensor for toxic Ni(II), Cd(II) and Hg(II) ions and bacteria, RSC Adv. 11 (2021) 22805.

[45] J.D. Zuo, S.M. Liu, Q. Sheng, Synthesis and application in polypropylene of a novel of phosphorus-containing intumescent flame retardant, Molecules 15 (2010) 7593–7602.

[46] C.N.R. Rao, Contribution to the infrared spectra of organosulphur compounds, Canadian J. Chem. 42 (1964) 36–42.

[47] L. Zhang, M. Yin, J. Qiu, T. Qiu, Y. Chen, S. Qi, X. Wei, X. Tian, D. Xu, An electrochemical sensor based on CNF@AuNPs for metronidazole hypersensitivity detection, Biosens. Bioelectron. 10 (2022), 100102.

[48] M. Shamsipur, L. Farzin, M.A. Tabrizi, F. Molaabasi, Highly sensitive label free electrochemical detection of VGEF$_{165}$ tumor marker based on "signal off" and "signal on" strategies using an anti-VEGF$_{165}$ aptamer immobilized BSA-gold nanoclusters/ionic liquid/glassy carbon electrode, Biosens. Bioelectron. 74 (2015) 369–375.

[49] E. Mohagheghpour, M. Rajabi, R. Gholamipour, M.M. Larijani, S. Sheibani, Correlation study of structural, optical and electrical properties of amorphous carbon thin films prepared by ion beam sputtering deposition technique, Applied, Surf. Sci. 360 (2016) 52–58.

[50] M. Panda, G. Mangamma, R. Krishnan, K. Madapu, D.N.G. Krishna, S. Dash, A. K. Tyagi, Nano scale investigation of particulate contribution to diamond like carbon film by pulsed laser deposition, RSC Adv. 6 (2016) 6016–6028.

[51] J. Li, D. Wu, Y. Yu, T. Li, K. Li, M.M. Xiao, Y. Li, Z.Y. Zhang, G.J. Zhang, Rapid and unamplified identification of COVID-19 with morpholino-modified graphene field-effect transistor nanosensor, Biosens. Bioelectron. 183 (2021), 113206.

[52] W.L. Ang, R.R.X. Lim, A. Ambrosi, A. Bonnani, Rapid electrochemical detection of COVID-19 genomic sequence with dual-function graphene nanocolloids based biosensor, FlatChem 32 (2022), 100336.

[53] Z. Fan, B. Yao, Y. Ding, J. Zhao, M. Xie, K. Zhang, Entropy-driven amplified electrochemiluminescence biosensor for RdRp gene of SARS-CoV-2 detection with self-assembled DNA tetrahedron scaffolds, Biosens. Bioelectron. 178 (2021), 113015.

[54] H. Zhao, F. Liu, W. Xie, T.C. Zhou, J.O. Yang, L. Jin, H. Li, C.Y. Zhao, L. Zhang, J. Wei, Y.P. Zhang, C.P. Li, Ultrasensitive supersandwich-type electrochemical sensor for SARS-CoV-2 from the infected COVID-19 patients using a smartphone, Sens. Actuator. B-Chem. 327 (2021), 128899.

[55] W. Heo, K. Lee, S. Park, K.A. Hyun, H.I. Jung, Electrochemical biosensor for nucleic acid amplification-free and sensitive detection of severe acute respiratory syndrome coronavirus 2 (SARS-CoV-2) RNA via CRISPR/Cas13a trans-cleavage reaction, Biosens. Bioelectron. 201 (2022), 113960.

[56] K. Zhang, Z. Fan, Y. Huang, Y. Ding, M. Xie, A strategy combining 3D-DNA Walker and CRISPR-Cas12a trans-cleavage activity applied to MXene based electrochemiluminescent sensor for SARS-CoV-2 RdRp gene detection, Talanta 236 (2022), 122868.

[57] K. Zhang, Z. Fan, Y. Huang, Y. Ding, M. Xie, M. Wang, Hybridization chain reaction circuit-based electrochemiluminescent biosensor for SARS-cov-2 RdRp gene assay, Talanta 240 (2022), 123207.

[58] B. Yao, J. Zhang, Z. Fan, Y. Ding, B. Zhou, R. Yang, J. Zhao, K. Zhang, Rational engineering of the DNA walker amplification strategy by using a Au@Ti$_3$C$_2$@PEI-Ru(dcbpy)$_3^{2+}$ nanocomposite biosensor for detection of the SARS-CoV–2 RdRp gene, ACS Appl. Mater. Interfaces 13 (2021) 19816–19824.

[59] G. Qiu, Z. Gai, Y. Tao, J. Schmitt, G.A. Kullak-Ublick, J. Wang, Dual-functional plasmonic photothermal biosensors for highly accurate severe acute respiratory syndrome coronavirus 2 detection, ACS Nano 14 (2020) 5268–5277.

[60] P. Moitra, M. Alafeef, K. Dighe, M.B. Frieman, D. Pan, Selective naked-eye detection of SARS-CoV-2 mediated by N gene targeted antisense oligonucleotide capped plasmonic nanoparticles, ACS Nano 14 (2020) 7617–7627.

[61] F.G. Banica, Chemical sensors and biosensors: Fundamentals and applications, Wiley, 2012.